Structure, Function, and Wavelength Selection in Blue-Absorbing Proteorhodopsin[†]

Jason R. Hillebrecht,[‡] Jhenny Galan,[‡] Rekha Rangarajan,[‡] Lavoisier Ramos,[‡] Kristina McCleary,[‡] Donald E. Ward,[§] Jeffrey A. Stuart,[∥,⊥] and Robert R. Birge*,[‡]

Departments of Chemistry and Molecular and Cell Biology, University of Connecticut, 55 North Eagleville Road, Storrs, Connecticut 06269-3060, Genencor International, Inc., 925 Page Mill Road, Palo Alto, California 94304-1013, and W. M. Keck Center for Molecular Electronics, Syracuse University, 111 College Place, Syracuse, New York 13244-4100

ABSTRACT: The absorption maximum of blue proteorhodopsin (BPR) is the most blue-shifted of all retinal proteins found in archaea or bacteria, with the exception of sensory rhodopsin II (SRII). The absorption spectrum also exhibits a pH dependence larger than any other retinal protein. We examine the structural origins of these two properties of BPR by using optical spectroscopy, homology modeling, and molecular orbital theory. Bacteriorhodopsin (BR) and SRII are used as homology parents for comparative purposes. We find that the tertiary structure of BPR based on SRII is more realistic with respect to free energy, dynamic stability, and spectroscopic properties. Molecular orbital calculations including full single- and double-configuration interaction within the chromophore π-electron system provide perspectives on the wavelength regulation in this protein and indicate that Arg-95, Gln-106, Glu-143, and Asp-229 play important, and in some cases pH-dependent roles. A possible model for the 0.22 eV red shift of BPR at low pH is examined, in which Glu-143 becomes protonated and releases Arg-95 to rotate up into the binding site, altering the electrostatic environment of the chromophore. At high pH, BPR has spectroscopic properties similar to SRII, but at low pH, BPR has spectroscopic properties more similar to BR. Nevertheless, SRII is a significantly better homology model for BPR and opens up the question of whether this protein serves as a proton pump, as commonly believed, or is a light sensor with structure−function properties more comparable to those of SRII. The function of BPR in the native organism is discussed with reference to the results of the homology model.

Proteorhodopsin (PR)[1] is the light-transducing protein found in the membranes of an uncultivated clade of *γ-proteobacteria* known as SAR86 (*5*, *6*). Since the initial discovery of PR in Monterey Bay (CA), several variants of the protein have been identified using environmental sequencing techniques (*21*, *22*). The two primary subgroups of PR are characterized in terms of absorption maxima as green-absorbing (GPR) or blue-absorbing (BPR) variants.

The GPR variants are generally found at the ocean surface and have absorption maximum near 525 nm. The BPR subgroup has an absorption maximum near 490 nm. The latter variants were originally detected in Antarctic waters and deep ocean samples (∼75 m) near the Hawaiian Ocean Time Station (*6*, *17*, *27*). The blue-shifted absorption maxima of the BPR subgroup coincides with the attenuated light energy available at depths greater than 50 m.

The absence of a cultivated host organism (SAR86) has led investigators to express variant forms of PR in *Escherichia coli* (*5*, *9*, *13*). The resulting protein is very stable and exhibits excellent photocyclicity, which suggests that it is folding properly despite heterologous expression. Flash photolysis studies indicate that both PR subgroups pump protons from the intracellular to the extracellular face of *E. coli* membranes and have led to the suggestion that both serve as proton pumps *in vivo* (*5*, *6*). BPR and GPR both have photocycles similar to bacteriorhodopsin, although the nature of the intermediate states is still unresolved (*7*, *9*, *15*, *27*). While the kinetic properties of the GPR photocycle closely resemble the bacteriorhodopsin (BR) photocycle, the BPR photocycle is slower. The 150 ms photocycle rate observed in BPR is roughly 10 times slower than the rate observed in GPR variants (∼15 ms) (*6*, *27*). The significant difference in photocycle kinetics may simply reflect the lower light levels available deeper in the ocean. However, the difference might be due to a functional difference between the proteins;

* To whom correspondence should be addressed. Telephone: 860-486-6720. Fax: 860-486-2981. E-mail: rbirge@uconn.edu.
[‡] University of Connecticut.
[§] Genencor International, Inc.
[∥] Present address: Department of Chemistry, University of Connecticut, 55 North Eagleville Road, Storrs, CT 06269-3060.
[⊥] Syracuse University.

[1] Abbreviations: PR, proteorhodopsin; GPR, green proteorhodopsin; BPR, blue proteorhodopsin; BR, bacteriorhodopsin; SRII, sensory rhodopsin II; IPTG, isopropyl-β-D-thiogalactopyranoside; EDTA, ethylenediaminetetraacetic acid; Ni−NTA, nickel−nitrilotriacetic acid; HEPES, *N*-2-hydroxyehtylpiperazine-*N*′-2-ethanesulfonic acid; TAPS, 3-[[tris(hydroxymethyl)methyl]amino]propanesulfonic acid; CAPS, 3-(cyclohexylamino)propanesulfonic acid; BLOSUM40, Block Substitution Matrix-40; MM3, molecular mechanics 3; MM2, molecular mechanics 2; ABNR, adopted basis Newton−Raphson; CHARMm, chemistry at Harvard molecular mechanics; TM, transmembrane; MNDO-PSDCI, modified neglect of differential overlap with partial single- and double-configuration interaction; CI, configuration interaction; SVD, singular-value decomposition.
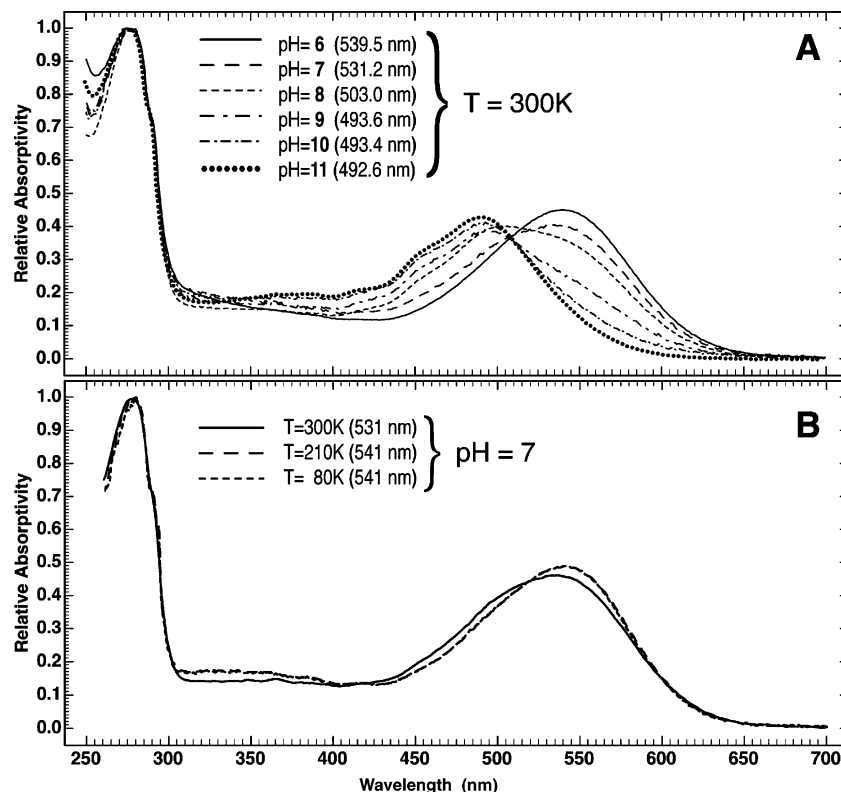
FIGURE 1: Absorption spectra of BPR (HOT75m1) as a function of pH at 300 K (A) and temperature at pH 7 (B). All spectra were normalized, and a baseline correction was added to the pH 6 spectrum in A to compensate for scattering because of partial association of the protein. The long-wavelength absorption maxima associated with the chromophore are listed in parentheses. Note that the absorption maximum shifts to the red and that the full width at half-maximum decreases upon lowering the temperature of the neutral pH spectrum (B). This result is in contrast to a temperature study at pH 11, which showed no observable change of the spectrum as a function of the temperature.

BPR might not be a BR-like proton pump but more akin to a photosensor, like sensory rhodopsin II (SRII). We discuss this issue in more detail below.

Previous homology-based studies of BPR and GPR were based on the use of BR as the homology parent (*17*). In this study, we explore the potential advantages of using SRII as the homology parent in modeling BPR. Although both BR and SRII exhibit comparable homology with respect to BPR, the SRII-based homology model has a significantly lower energy and is more stable to long-term molecular dynamics using either quantum mechanical or molecular mechanical Hamiltonians. We conclude that the SRII-based homology model provides a more realistic starting point for structure−function studies and provides greater insight into spectral tuning and the unique vibronic structure observed in the absorbance profile of BPR. The success of SRII as a homology model coupled with the low efficiency of the BPR photocycle suggests the possibility that BPR may serve a sensory rather than energy-transducing role in the native host.

MATERIALS AND METHODS

Preparation and Purification of BPR. The PR genes (HOT75m1) were amplified and cloned into *E. coli* using the pTrcHis2 TOPO TA Expression Kit (Invitrogen, Carlsbad, CA). A C-terminal His tag was added to the BPR constructs to facilitate purification of the protein. The BPR expression plasmids were transformed into BL21-Codonplus-RIL cells and grown in LB media containing 0.5% glucose, 100 μg/mL of carbenicillin, and 10 μM all-*trans* retinal at

37 °C. The BPR constructs were then expressed by adding 0.5 mM isopropyl-β-D-thiogalactopyranoside (IPTG) and 10 μM all-*trans* retinal for an additional 4 h of growth at 37 °C. The cells were harvested via centrifugation at 3500g (10 min) and freeze-dried at −80 °C. A more thorough description of this procedure is reported in Kelemen et al. (*13*).

The membrane fraction of the BL21-Codonplus-RIL cells was isolated by resuspending the cell paste in a lysis buffer containing 50 mM Tris (pH 7.7), 0.5 M ethylenediaminetetraacetic acid (EDTA) (pH 8.0), and 0.2 mg/mL lysozyme. The lysates were homogenized using a French press, and the membrane fraction was purified from the cellular debris via multiple low- and high-speed centrifugation spins for 30 min at 4 °C. A buffer containing 50 mM Tris (pH 7.7) and 2% dodecyl-β-D-maltoside was then used to resuspend the membrane fraction prior to a second, more thorough, homogenization using a tissue homogenizer. The protein was then isolated from the membrane via fractionation in a nickel−nitrilotriacetic acid (Ni−NTA; Amersham) binding resin column and dialyzed and concentrated using dialysis tubing (12 → 14 kDa) and a 30-kDa Amicon membrane filter, respectively.

Absorption Spectroscopy. Absorption spectra of BPR at pH values from 6 to 12 were collected by suspending the protein (5 μL of 11 mg/mL) in 500 μL of buffer containing 100 mM phosphate (pH 6.0 and 12.0), *N*-2-hydroxyehtylpiperazine-*N*′-2-ethanesulfonic acid (HEPES) (pH 7.0), 3-[[tris-(hydroxymethyl)methyl]amino]propanesulfonic acid (TAPS) (pH 8.0), and 3-(cyclohexylamino)propanesulfonic acid
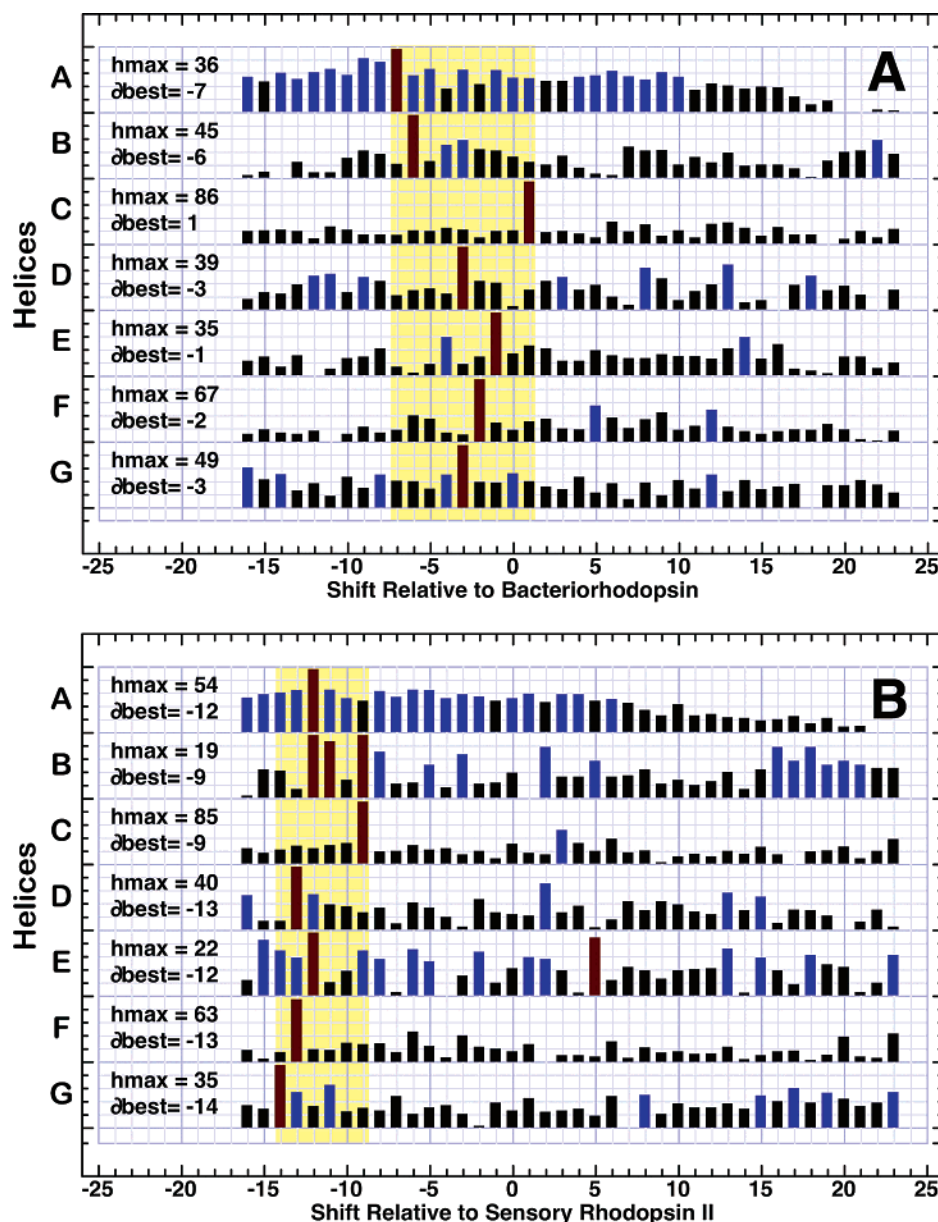
FIGURE 2: Homology analysis of the primary sequence of BPR (accession number Q9AFF7) relative to the polypeptide sequences of BR (1C3W based) in A and SRII (1H68 based) in B. The BLOSUM40 matrix was used to align the coding sequence of BPR with the BR and SRII parent. The helical regions of the template sequence (BR or SRII) are shown on the vertical axis as A−G. Red bars indicate the maximum homology scores for each alignment, and blue bars indicate good homology, while black bars indicate lower scores. To achieve the maximum homology score (h_{max}), the sequence alignment is shifted by a variable number of residues ($\partial best$), relative to the original sequence frame. The range of shifts necessary to achieve maximal homology is indicated by a yellow background.

(CAPS) (pH 10.0 and 11.0). A Cary50 scan spectrophotometer (Varian, Inc., Palo Alto, CA) was used to collect UV−vis spectra from 250 to 750 nm (*13*). The spectra for all samples were collected at ambient temperature. For experiments conducted at lower temperature, the samples contained 67% glycerol. The BPR sample in 67% glycerol was placed in a helium-refrigerated cryostat (APD Cryogenics, Inc.) connected to a Cary50 UV−vis spectrophotometer (Varian, Inc., Palo Alto, CA). The protein sample was equilibrated at the set temperature (∼80 K) for 1 h. All spectra were normalized on the basis of the absorbtivity of the long-wavelength maximum. The spectrum collected at pH 6 and 300 K was corrected for scattering because of protein aggregation. The results are shown in Figure 1.

Homology Modeling. The BPR primary sequence (accession number Q9AFF7) was aligned with the polypeptide sequences of the SRII (1H68) and the BR (1C3W) crystal structures by using the BLOSUM40 (Block Substitution Matrix-40) scoring matrix (*10*, *11*, *26*). The BLOSUM40 scoring matrix assigns a homology score to each of the transmembrane (TM) regions of the protein, as shown in parts A and B of Figure 2.

Maintaining a high homology score for each TM region was the primary goal during the construction of the sequence alignments. The initial 26 residues (MGKLL LILGS AIALP SFAAA GGDLD I) or 25 residues (MGKLL LILGS AIALP SFAAA GGDLD) of the BPR sequence were ignored to align the BPR sequence with the crystal structures of SRII (1H68)

```
BR:    5     tgrpewiwlalgtalmglgtlyflvkgmgvsdpdakkfyaittlvp
             :    : : |  || |   :|::|:|:    ||   : |   :::: |:
BPR:  26     isdtvgvsfwlvtagmlaatvfffverdqvs~akwktsltvsglit


BR:   51     aiaftmylsmllgygltmvpfggeqnpiywaryadwlfttplllld
             :|||  :|| |      :   |          :    █|  █||:|:|| :::
BPR:  71     giafwhylymrgvwidt~~~~~~~gdtptvfryidwlltvplqvve


BR:   97     lallvdad****qgtilalvgadgimigtglvgaltkvysyrfvww
             :   |:: |      :   |:::: :|:|:|::|     ::   :
BPR: 110     fylilaactsvaaslfkkllagslvmlgagfageag~~lapvlpaf

                                   *****
BR:  139     aistaamlyilyvlffgf*tskaesmrpevastfkvlrnvtvvlws
             |: |:  || ::|  |::|        :   |  |  |:::::   :  || |:
BPR: 154     iigmagwlymiyelymgegkaavstaspavnsaynammmiivvgwa


BR:  184     aypvvwligseg*agivplnietllfmvldvsakvgfglillrsra
             ||: :   :   :  |   :  |:  |  █: |   █:  |||| :  :
BPR: 200     iypagyaagylmggegvyasnlnliynladfvnkilfgliiwnvav


BR:  229     ifg
             :
BPR: 246     kes
                                                              A


SRII:  1     mvglttlfwlgaigmlvgtlafawagrdagsgerryyvtlvgisgi
             :  :  ||| : |||::|: |       ::::   :: ::|:  : |
BPR:  27     sdtvgvsfwlvtagmlaatvfffverdqvsa~~~kwktsltvsgli


SRII: 47     aavayvvmalgvgwvpvaertvfapryidwilttplivyflgllag
             :::|:  :  :  |   █||█:||:||:|| |    : |: :
BPR:  70     tgiafwhylymrgvwidtgdtptvfryidwlltvplqvvefylila


SRII: 93     *lds***refgivitlntvvmlagfagamvpgieryalfgmgavaf
             |        |    ::: :  |:: |||||      :  :   |  :|  :::
BPR: 116     actsvaaslfkkllagslvmlgagfageagl~apvlpafiigmagw


SRII: 136    lglvyylvgpmtesa*sqrssgikslyvrlrnltvilwaiypfiwl
             |  ::| |        ::| |   |  :::| |   :   : |: |||||   :
BPR: 161     lymiyelymgegkaavstaspavnsaynammmiivvgwaiypagya


SRII: 181    lgppg*valltptvdvalivyldlvtkvgfgfialdaaatlraeh
             |       :   :    ::: : █:|:█: ||:|  ::|:    ::
BPR: 207     agylmggegvyasnlnliynladfvnkilfgliiwnvavkessna
                                                              B
```
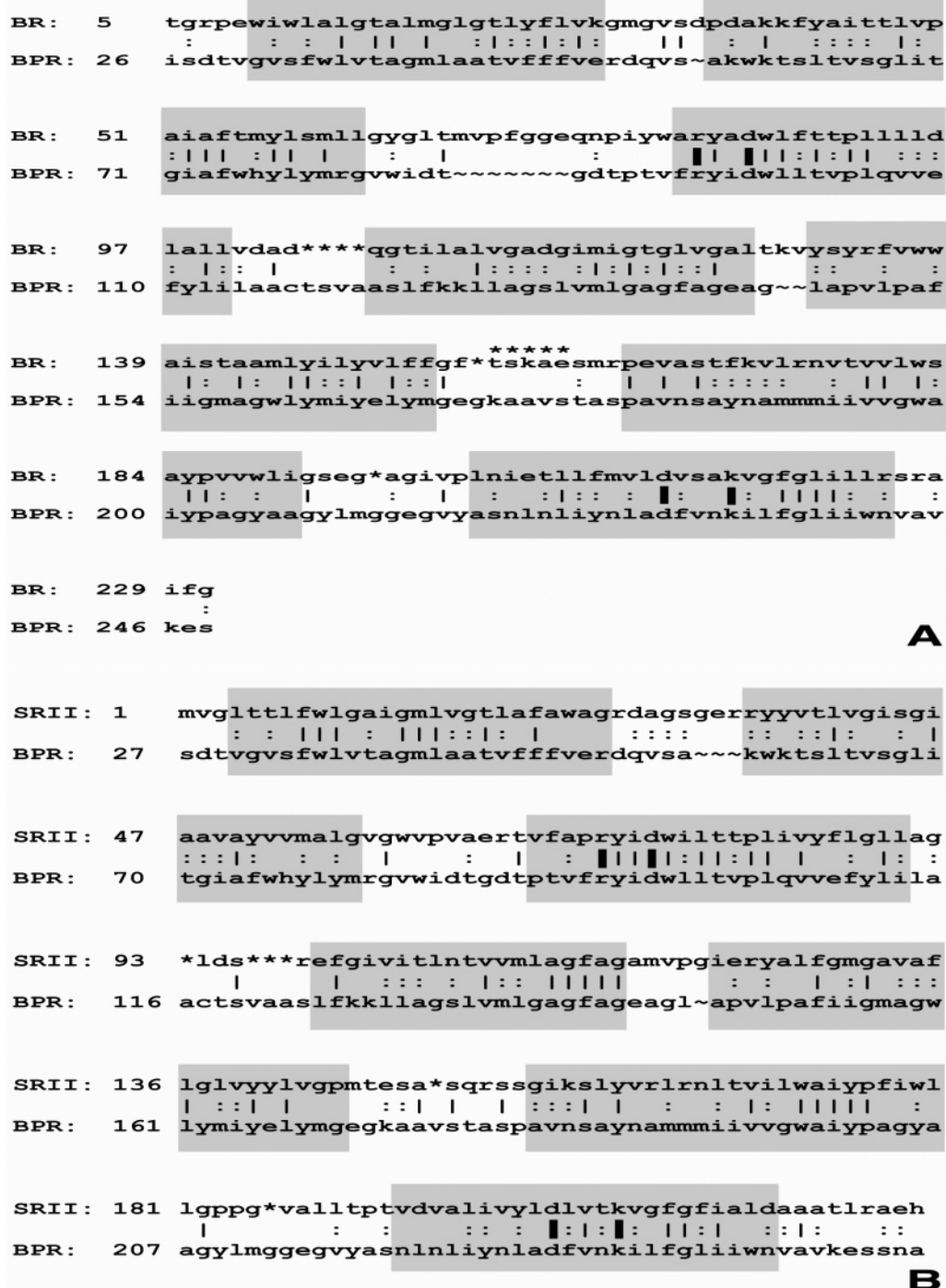
FIGURE 3: Linear sequence alignment of BPR versus BR (A) and SRII (B). The gray shaded blocks represent the helical regions of the alignment profile, on the basis of the 1C3W (BR) and 1H68 (SRII) crystal structures. The alignment files contain several identical residues that are defined by a vertical dash (|), whereas conserved substitutions are identified by a colon (:). Bold dashes (|) indicate residues that are frequently conserved in retinylidene proteins. Residue deletions (~) and insertions (*) were required to preserve the maximum homology score for each TM region of the alignment. Note that several residues in A contain an asterisk above the amino acid letter code. These are BR residues that are not present in the 1C3W crystal structure. To align 1C3W with the primary sequence of BPR, residue insertions (*) were required for these "omitted" positions.

and BR (1C3W), respectively. In each case there was a single linear alignment that provided maximal homology as shown in parts A and B of Figure 3. All three proteins have well-defined loop and TM regions as illustrated by the Kyte–Doolittle plots of Figure 4. As we will discuss in more detail below, however, the data shown in Figures 2–4 suggest that SRII may provide a better homology model for BPR.

All of the modifications (residue insertions and deletions) to the loop regions were temporary and restored to the original BPR sequence following an initial energy minimization of the model. No penalties were assigned for the manipulation of loop residues (insertion or deletion). A homology profile for the SRII- and BR-based alignment of BPR was generated in an alignment program developed in-
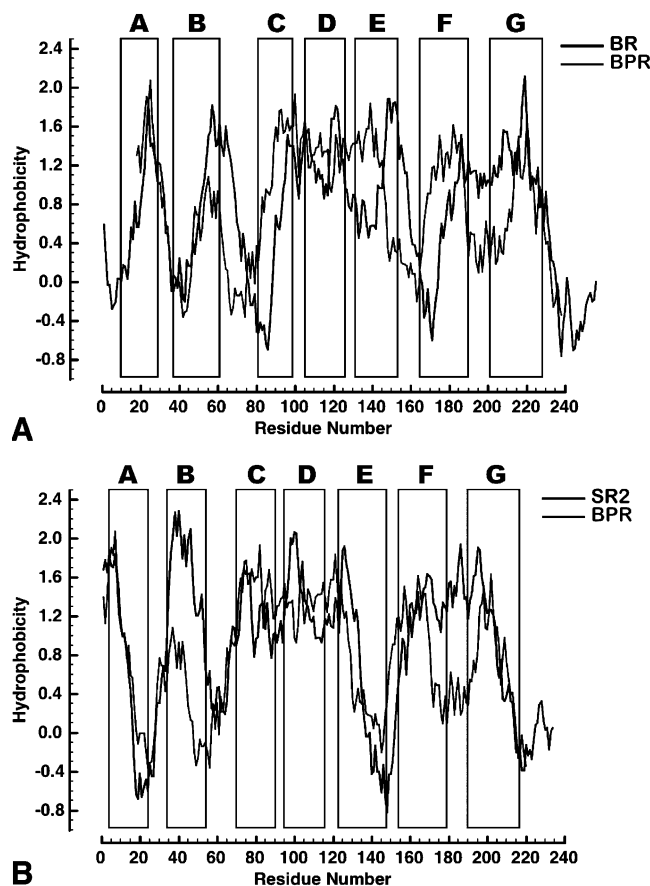
FIGURE 4: Kyte–Doolittle hydrophobicity plots of the primary sequence of BPR relative to the BR (A) and SRII (B) coding sequences. The gray blocks represent the TM regions of BR or SRII, on the basis of sequence data gathered from the 1C3W and 1H68 crystal structures, respectively. The initial 25 residues of BPR were omitted to provide maximum alignments with the primary structures of the parental templates.

house, which may be obtained from the corresponding author upon request. The residue insertions and deletions shown in each homology profile (parts A and B of Figure 2) are consistent with the linear sequence alignments (parts A and B of Figure 3). Bold vertical bars were used in parts A and B of Figure 3 to denote the amino acids that serve a key functional role in retinylidene ion pumps and sensory proteins. A two-dimensional rendering of the BPR primary sequence is also shown in Figure 5A.

The SRII- and BR-based linear alignment files were then independently read into the Cache-6.1.1 sequence manager using 1H68 and 1C3W as structural templates, respectively (*16*, *20*). The charge assignments for Arg-95 (+), Asp-98 (−), Asp-229 (−), and Lys-233 (+) are analogous to the protonation states observed in the BR resting state. All ionic residues were neutralized to avoid incorrect charge assignment for residues lacking accurate pK_a data (*19*). Accurate valence and hybridization was confirmed for each residue by hand using Cache. Energy minimizations were performed on each model using the molecular mechanics 3 (MM3) module in Cache-6.1.1. The steepest descent method was used to minimize each model to a convergence value of 0.001 kcal/mol Å. The structure was then refined using the conjugate-gradient method described by Allinger (*2*, *4*). A fixed peptide backbone and a cutoff distance of 9 Å were maintained for all MM3 calculations.

Following the initial energy minimizations (MM3, steepest descent/conjugate gradient), the loop regions of each model were modified (residue insertions and deletions) to restore the identity of the original BPR sequence. A molecular mechanics 2 (MM2) calculation was then used to relax the conformation of each modified loop, while the remainder of the protein was locked in a fixed position. MM2 calculations underestimate the carbon–carbon barriers in congested molecules by approximately 40%, relative to the MM3 module (*1*, *3*). The added freedom of motion allowed the loop regions to relax into stable conformations.

Following the reconstruction and minimization of the loop regions, the SRII- and BR-based models were minimized by using 4000 cycles of steepest descent using ABNR (adopted basis Newton–Raphson). Harmonic constraints were applied to the backbone of the protein during the ABNR minimization ($k = 10.0$ kcal/mol Å^2). The systems were then heated to 300 K for 20 ps, followed by 100 ps of equilibration at the same temperature. The equilibrated structures were then subjected to molecular dynamics simulations for 2 ns (1 fs time step). Harmonic constraints were applied to the backbone during the molecular dynamics simulation. A nonbonded cutoff of 15 Å was used with switch nonbonding smoothing and a dielectric constant of 1.0 for all calculations. All molecular dynamics calculations assumed NVT conditions (canonical ensemble) and were based on the leap Verlet algorithm. The molecular dynamics calculations were carried out using CHARMm [(c29b2) Charmm22 parameter set for proteins, and TIP3P model set for water molecules]. Chromophore parameters were adapted from optimized all-*trans*-retinyl-protonated Schiff-base parameters published by Hermone and Kuczera (*12*).

The relative energies for the TM regions of the BPR homology models were calculated using previously minimized structures (2 ns molecular dynamics simulation). A separate parameter structure file was created for the TM regions of each model using the same coordinates as the 2 ns structures. The parameter structure file contains all of the information necessary for energy evaluation (*8*). The potential energy of the TM regions was calculated using the energy evaluation function implemented in CHARMm (*8*). The potential energy function in CHARMm includes bonding (bond stretches, bond angles, and dihedral-angle contributions) and nonbonding (van der Waals and electrostatic interactions) interactions between pairs of atoms.

Molecular Orbital Theory. The modified neglect of differential overlap with partial single- and double-configuration interaction (MNDO-PSDCI) molecular orbital theory was used to calculate the spectroscopic properties of the SRII- and BR-based retinal-binding sites of BPR (*18*, *19*). To predict the spectroscopic properties of each homology model, the PM3 parametrization was selected because of its more reliable description of water- and protein-bound chromophores relative to the AM1 parametrization (*19*, *24*). The configuration interaction calculation included full single- and double-configuration interaction (CI) within the retinal chromophore π system. The binding site was simulated by including all residues and water molecules within 5.6 Å of any chromophore atom and any ionic residues within 12 Å (*19*). When dispersion was included in the calculation, only the aromatic residues in the first shell of the protein-binding site were included (F48, F74, W99, F153, W160, W198,
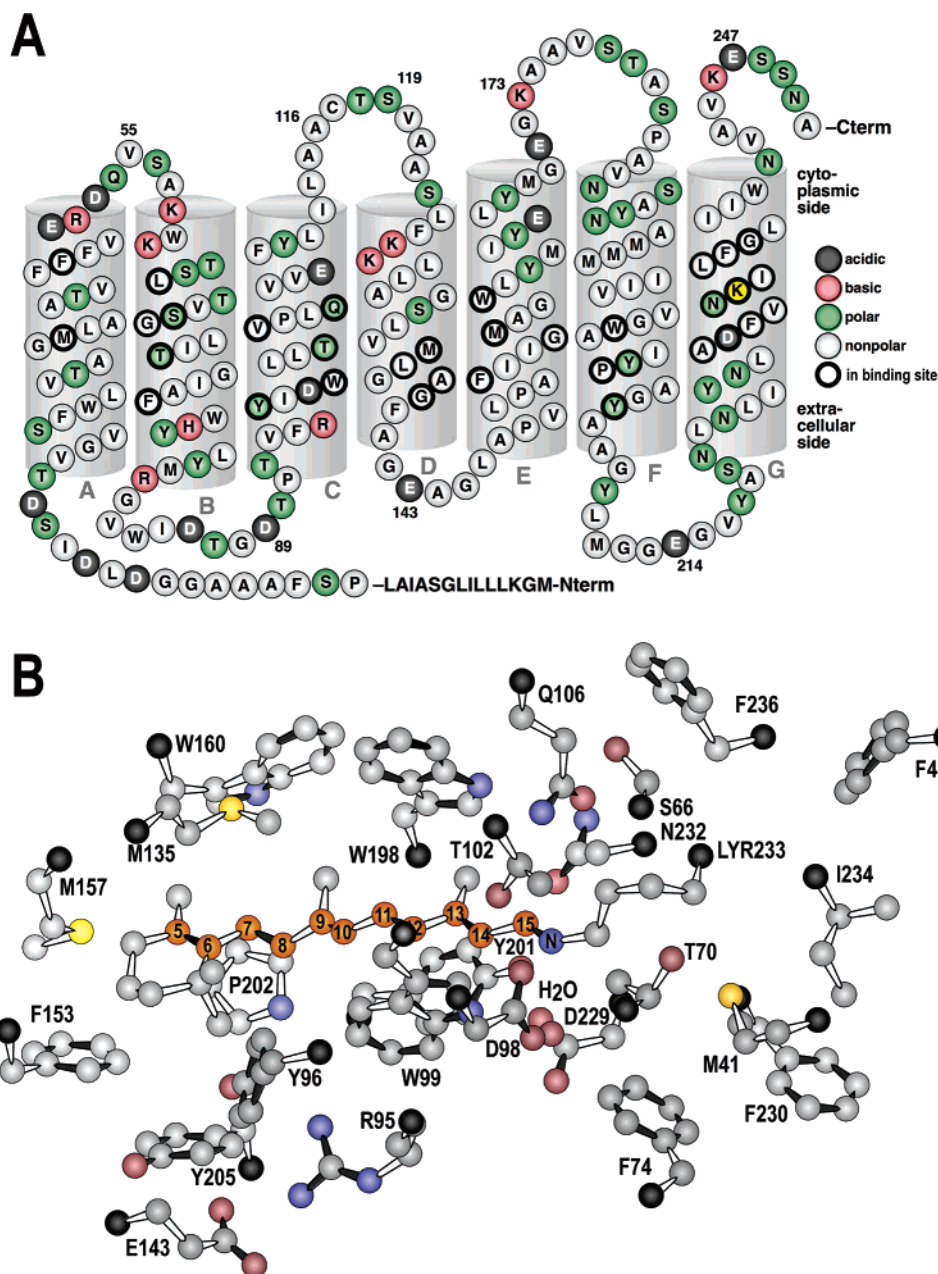
FIGURE 5: Primary sequence (A) and selected binding site residues (B) resulting from the SRII-based homology model of BPR. Thicker circles in A indicate residues that are in the first shell of the chromophore-binding site. The binding site is calculated to have a refractive index of 1.5024. Note that Tyr-201 (Y201) is obscured behind Trp-99 (W99) and Asp-98 (D98). Arg-95 (R95) and Glu-143 (E143) are not in the first shell but were included for spatial reference. α carbons are shown in black.

Y201, and F230; see Figure 5B). Dispersion was introduced using the same computational approach as detailed in ref *19*. Our molecular orbital procedures are in all other respects identical to those used in previous studies of protein-binding sites (*14, 19, 24*).

RESULTS

Absorption Spectroscopy of Purified BPR. The absorption spectra for wild-type BPR (HOT75m1) were collected at ambient temperature (300 K) and as a function of pH (Figure 1A). Absorption spectra were also collected at low temperature (210 and 80 K), as shown in Figure 1B. All spectra were normalized, and a baseline correction was added to the pH 6 spectrum in Figure 1A to compensate for scattering because of partial association of the protein. Titrating BPR

produced a spectral shift of ~50 nm, with a modest vibrational structure observable at alkaline pH.

Singular-value decomposition (SVD) of the ambient temperature pH-dependent spectra (Figure 1A) indicates that there are two regions with different decomposition characteristics. The λ_{max} region from 400 to 650 nm has a simple two-component decomposition, which suggests that the lack of a clear isosbestic point in Figure 1A is due to baseline problems rather than higher order populations. In contrast, the aromatic region from 250 to 320 nm decomposes into three components, which suggests that two or more aromatic residues are affected by the pH-induced changes in the protein tertiary structure.

Homology Modeling. Aligning the seven TM regions of BR and SRII with the primary sequence of BPR yielded a

Table 1: Relative Energies of BPR Calculated for BR- and SRII-Based Homology Models[a]

model	total energy	internal energy	van der Waals	electro-static
BPR_BR (TM)	0[b]	0[c]	147	−762
BPR_SRII (TM)	−15 651[b]	−15262[c]	−239	−765
BPR_BR (min, TM)	−3796[b]	−3900[c]	243	−754
BPR_SRII (min, TM)	−21 351[b]	−21 115[c]	−42	−810
BPR_BR (min, all)	−2062	3754	5	−6002
BPR_SRII (min, all)	−3235	2719	−202	−6085

[a] All energies are in kcal/mol and were calculated after a 2 ns molecular dynamics simulation using CHARMm (see the Materials and Methods). When "(TM)" is indicated, the energies are calculated only for those residues in the TM segments (see Figure 5A), whereas "(all)" indicates the entire protein. When "(min)" is indicated, the energies are for a 2 ns molecular dynamics simulation followed by a minimization. Models of BPR based on BR are listed as BPR_BR and those based on SRII are listed as BPR_SRII. [b] Total energies relative to the BPR_BR (TM) model, which had the largest total energy of the TM structures. [c] Internal energies calculated relative to the BPR_BR (TM) model, which had the largest internal energy of the TM structures.

homology score of 0.29 (BLOSUM40 scoring matrix). Because of the variable number of amino acids in the loop regions of SRII and BR, each TM region of the protein was aligned individually. Aligning the TM regions of the BR- and SRII-based alignment profiles required that residue shifts be used to achieve the maximum homology score (h_{max}). The residue shifts used for the BR- and SRII-based alignment files are shown in Figures 2 and 3. In the case of the BR-based alignment profile (Figure 2A), helices A and B were shifted by an additional 3−4 residues, relative to helices C → G. While the net shift for the comparison to BR is smaller than for that of SRII, the overall width of the band for the latter is smaller. The bandwidth of both homology models is highlighted in yellow in Figure 2.

Despite the differences cited above, both BR and SRII provide excellent homology models for BPR in the TM regions. In conjunction with the sequence-alignment profiles, Kyte−Doolittle plots were used to compare the relative hydrophobicity of BPR with the primary structure of BR and SRII. The Kyte−Doolittle plots in Figure 4A (BR versus BPR) and Figure 4B (SRII versus BPR) illustrate that seven distinct hydrophobic regions exist in the BPR polypeptide sequence.

The construction of the BPR homology models was followed by a series of energy minimizations and molecular dynamics simulations. The relative potential energies of the 2 ns structures and the minimized 2 ns structures are shown in Table 1. In all cases, the SRII-based models are lower in energy by significant values. More importantly, inspection of the binding sites predicted by the two-homology models indicates that the BR-based model undergoes a partial collapse after 2 ns dynamics. The collapse involves the formation of a strong salt bridge between the chromophore and Asp-229 as shown in Table 2. The distances shown in Table 2 were measured between the Schiff-base nitrogen of the retinal chromophore and the carboxyl oxygens (OD1 and OD2) on Asp-98 and Asp-229. In the BR-based model, Asp-229 (OD1) is located 2.67 Å from the Schiff-base linkage, whereas the same atom is separated by a distance of 3.14 Å in the SRII-based model. Performing identical dynamics simulations on the 1C3W crystal structure of BR yielded a far more reasonable binding pocket, with Asp-212 (OD1)

Table 2: Distances Measured between the Schiff-Base Nitrogen of the Retinal Chromophore and the Carboxylate Oxygen Atoms on nearby Counterions

	distance (Å)		
protein/atoms[a]	crystal structure[b]	after 2 ns MD	stability[c]
rhodopsin (1U19)			(+)
NZ(Ret): OE1 E113	3.45	3.11	
NZ(Ret): OE2 E113	3.71	3.70	
BR (1C3W)			(+)
NZ(Ret): OD1 D85	3.79	2.97	
NZ(Ret): OD2 D85	4.38	4.35	
NZ(Ret): OD1 D212	3.74	4.42	
NZ(Ret): OD2 D212	4.87	5.34	
BPR−BR E143			(−)
NZ(Ret): OD1 D98		4.90	
NZ(Ret): OD2 D98		5.78	
NZ(Ret): OD1 D229		2.67	
NZ(Ret): OD2 D229		4.87	
BPR−SRII E143 (−)			(+)
NZ(Ret): OD1 D98		4.71	
NZ(Ret): OD2 D98		5.05	
NZ(Ret): OD1 D229		3.14	
NZ(Ret): OD2 D229		4.58	
BPR−SRII E143			(+)
NZ(Ret): OD1 D98		3.61	
NZ(Ret): OD2 D98		4.26	
NZ(Ret): OD1 D229		4.19	
NZ(Ret): OD2 D229		5.51	

[a] The protein is designated by the Protein Data Bank entry (crystal structure) or the homology-based protein followed by the homology parent. The distance measurements are between the Schiff-base nitrogen [NZ(Ret)] of the retinal chromophore and the two carboxylate oxygen atoms on the nearby aspartic (glutamic for Rho) acid counterions. The OD1 (OE1 for Rho) designation is assigned arbitrarily to the oxygen atom closer to the Schiff-base nitrogen atom. E143 is either neutral or negatively (−) charged. [b] Interresidue atomic distances were calculated for the crystal structures prior to and following a 2 ns molecular dynamics simulation (see the Materials and Methods). [c] Stability is indicated with a +; instability is indicated with a −; and in the case of the BR E143 model, the instability results in a collapsed binding site (see the text).

located 4.42 Å from the Schiff-base linkage. We conclude from this observation alone that the BR-based model is neither stable nor realistic. One significant aspect of the SRII-based model is that Arg-95 starts out in a downward position as in the SRII parent. The Arg-95 residue is stable in this position provided that the Glu-143 residue is negatively charged (Figures 5 and 6). However, if Glu-143 is neutral, Arg-95 migrates up into the binding site as discussed in more detail below. Glu-143 is not at the extracellular surface, as implied by Figure 5A, but surrounded by residues populating the DE and BC loops as depicted in Figure 6. Nevertheless, inspection of this region of the protein suggests that the water from the extracellular medium will have direct access to Glu-143, a fact that is important in our examination of the effect of pH on the absorption spectrum (see below).

Molecular Orbital Calculations. The MNDO-PSDCI energies and intensities of the low-lying $\pi\pi^*$ states of the chromophore in the SRII- and BR-based models of BPR are shown in parts A and B of Figure 7, respectively. The predicted low-lying $\pi\pi^*$ states of the chromophore have been superimposed on the absorption spectra of BPR at high (11) and low (6) pH. The MNDO-PSDCI calculations overestimate the transition energy of the $^1B_u^{*+}$-like state regardless of the homology model, in part because of a neglect of dispersion in this set of calculations. However, the BR-based
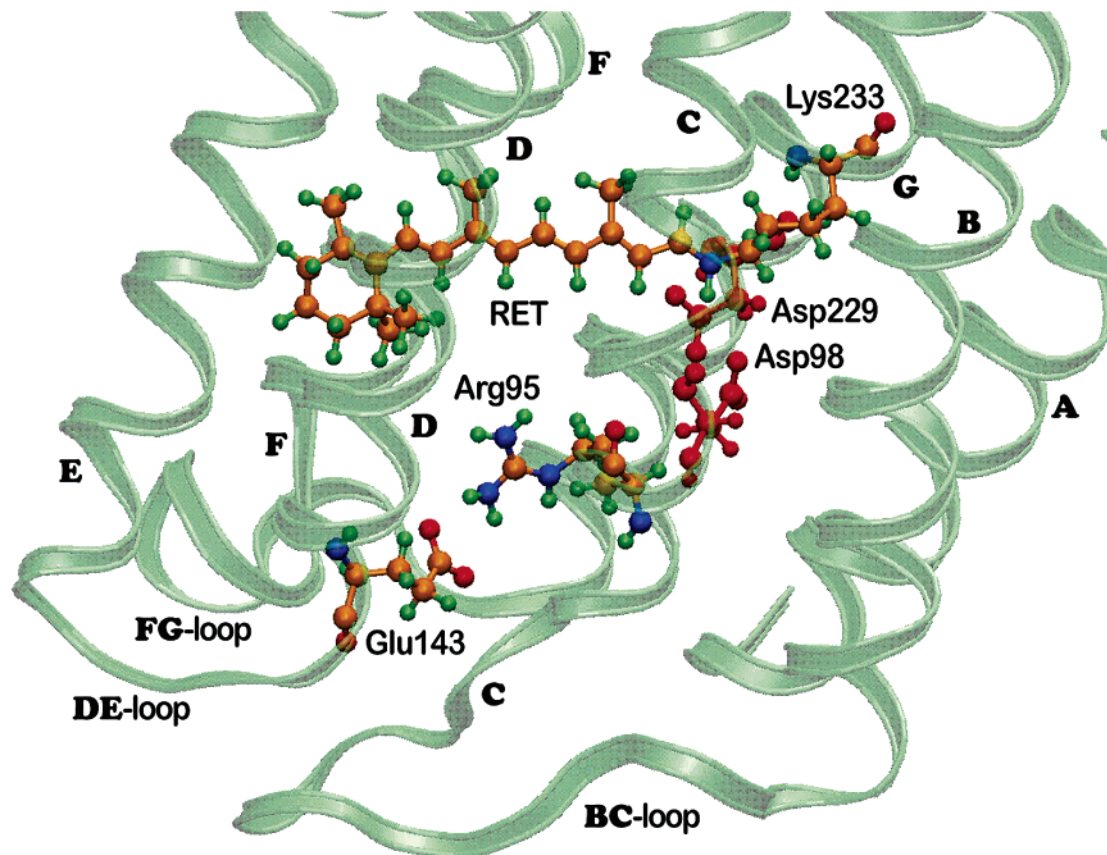
FIGURE 6: Helix backbone and selected residues of the SRII-based homology model of BPR. The helices are labeled as in Figure 4A, and the key extracellular loops are indicated. Note that, while Glu-143 is attached to the DE loop, the BC loop extends below this residue and provides partial buffering of Glu-143 from the extracellular medium.

model generates a transition energy that is significantly higher than observed and a level ordering that places the $^1A_g^{*-}$-like state below the $^1B_u^{*+}$-like state. This level ordering is highly unlikely and can be traced to a collapsed binding site.

Figure 8 compares the electronic transitions observed in the SRII-based model of BPR with comparable MNDO-PSDCI calculations performed previously on SRII (*Np*SRII) and BR (light-adapted) (*19*). Dispersion effects were included for all of the simulations shown in Figure 8 to more accurately reflect the photophysical contributions of the aromatic residues in the binding site. Nevertheless, all three simulations predict a low-lying strongly allowed state that is blue-shifted relative to the observed λ_{max} band. We suggest that this is associated with a basic limitation inherent in our use of semiempirical methods. The intensities of the $^1B_u^{*+}$-like states are relatively consistent for all three spectra. However, the MNDO-PSDCI calculations predict a $^1A_g^{*-}$-like state for the BPR model (Figure 8A) with significantly less intensity than its counterpart in *Np*SRII (Figure 8B). The BR-based homology model was not included in Figure 8 because of the unreasonable energy states predicted by the MNDO-PSDCI calculations.

DISCUSSION

SRII- and BR-Based Homology Structures. System energies calculated via molecular mechanics have no absolute relevance. However, the difference in calculated potential energy is useful in comparing the relative stability of two or more conformations. As shown in Table 1, the molecular

dynamics simulations predict that the minimized TM regions of the SRII-based homology model possess a lower potential energy than its BR-based counterpart. Because of the varying lengths of the loop regions of the BR (1C3W) and SRII (1H68) crystal structures, the highly conserved TM regions were used for comparison purposes. These data suggest that the SRII parent structure provides a more accurate conformation of BPR, relative to that generated by the BR-based model. In this section, we investigate the key structural differences between the BR- and SRII-based BPR homology models and examine their relative advantages and disadvantages in explaining the photochemical and spectroscopic properties.

A structural analysis of the BPR homology models revealed discrepancies in the orientation and position of certain ionic residues lining the retinal-binding pocket, namely, Asp-229 and Arg-95. During a 2 ns dynamics simulation in the BR-based BPR homology model, Asp-229 collapses onto the protonated Schiff-base linkage of the chromophore, as shown in Table 2. The collapse of the charged counterion complex in the BR-based model is in stark contrast to the distances measured prior to and after molecular dynamics simulations carried out on the 1C3W and 1U19 crystal structures of BR and rhodopsin, respectively. The distances shown in Table 2 for the 1C3W and 1U19 simulations support the reliability of using molecular dynamics to model the retinal-binding pockets of the BPR homology models.

The BR analogue of Asp-229, Asp-212, is a key contributor to the stability of the charged counterion complex of the
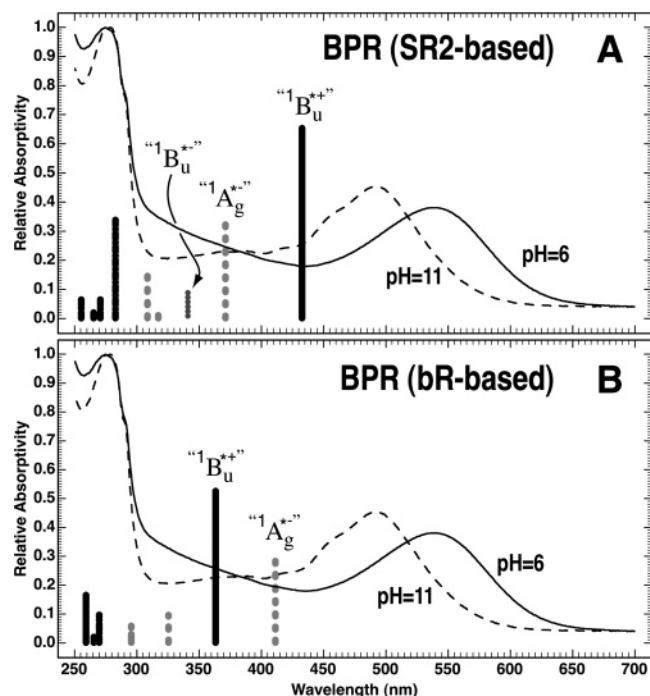
FIGURE 7: Calculated energies, relative oscillator strengths, and approximate symmetries of the low-lying $\pi\pi^*$ states of the chromophore have been superimposed on the absorption spectra of BPR at high (11) and low (6) pH. The low pH spectrum was not baseline-corrected for scattering because of slight protein aggregation. The relative oscillator strengths are represented by the height of the vertical line. The binding sites of the SRII-based (A) and BR-based (B) homology models were simulated by including all residues and water molecules within 5.6 Å of any chromophore atom and any ionic residues within 12 Å. Dispersion was not included in the calculations.

protein. Not surprisingly, the MNDO-PSDCI calculations on the collapsed BR-based binding pocket resulted in unrealistic spectroscopic properties. As shown in Figure 7B, the collapse of the retinal-binding pocket in the BR-based structure yields an unrealistic calculated transition for the $^1B_u^{*+}$-like state. The assignment of the $^1B_u^{*+}$-like state in the BR- (Figure 7B) and SRII- (Figure 7A) based calculation is the most prominent discrepancy between the two MNDO-PSDCI output files. This occurrence is most likely the result of the unrealistic counterion environment present in the BR-based structure.

The molecular dynamics simulations performed on the SRII-based homology model resulted in a more stable counterion complex, with Asp-98 and Asp-229 positioned more than 3.0 Å from the Schiff-base linkage of the chromophore, as shown in Figure 6. The MNDO-PSDCI calculations on the SRII-based model also appear to overestimate the energy of the symmetry assignments, as shown in Figure 7A. This observation is a reflection of the semiempirical nature of our procedures. Previous studies have shown that MNDO-PSDCI calculations overestimate the oscillator strength of the $^1A_g^{*-}$-like state when it is calculated to be close in energy to the $^1B_u^{*+}$-like state (19). Subsequent MNDO-PSDCI calculations used dispersion effects to mimic the spectral contributions of the entire apoprotein, as shown in Figure 8. Note that the MNDO-PSDCI calculations overestimate the energy of the lowest-lying strongly allowed excited singlet state in the SRII-based homology model (Figure 8A), *Np*SRII (Figure 8B), and light-adapted BR
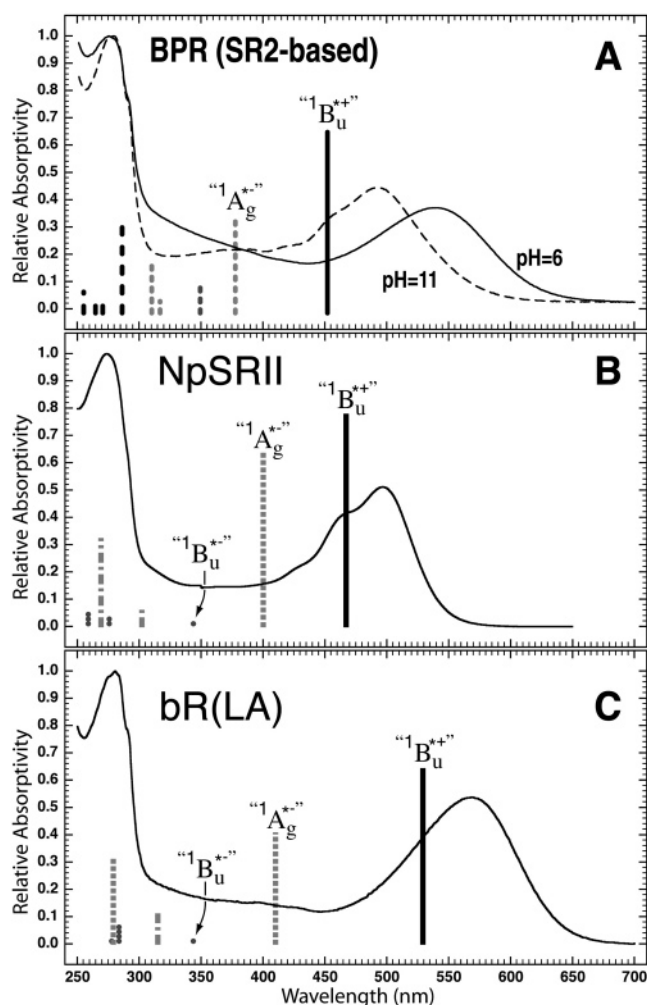

FIGURE 8: Calculated energies, relative oscillator strengths, and approximate symmetries of the low-lying $\pi\pi^*$ states of the chromophore have been superimposed on the absorption spectra of BPR (A, from Figure 6), *Np*SRII (B, *16*) and light-adapted BR (C, *16*). Dispersion effects involving the aromatic residues are included for the three binding site molecular orbital calculations (see the Materials and Methods).

(Figure 8C) by similar amounts. However, the calculated $^1B_u^{*+}$-like state in the SRII-based model (Figure 8A) is blue-shifted by approximately 10 nm, relative to the $^1B_u^{*+}$-like state observed in *Np*SRII (Figure 8B). This finding is consistent with the difference in the λ_{max} of BPR (490 nm) and *Np*SRII (498 nm) (*6, 25*).

Another notable difference in the counterion environment of the BPR homology models is the orientation and position of Arg-95. Previous investigations have shown that Arg-72 (SRII analogue to Arg-95) and its electrostatic interaction with Asp193 contribute to the fine vibrational structure and blue-shifted absorbance spectrum of *Np*SRII (*19*). The 2 ns molecular dynamics simulations predict that the guanidinium group of the Arg-95 side chain becomes oriented toward the protonated Schiff-base linkage of the chromophore in the BR-based model. This conformation is in stark contrast to the outward orientation of the Arg-95 side chain in the SRII-based model. The outward orientation of Arg-95 in the SRII-based model places the guanidinium group in close proximity (<2.5 Å) to Glu-143, an electronic environment that closely resembles the retinal-binding pocket of *Np*SRII. As mentioned above, the electrostatic interaction occurring between

Arg-95 and Glu-143 may explain the spectral shift observed for BPR under alkaline conditions.

Role of Gln-106 in Spectral Tuning. Experimental studies have demonstrated that Gln-106 plays an important role in the wavelength regulation of BPR (*17, 27*). This residue is replaced by leucine in GPR, and mutations of both GPR and BPR involving this residue indicate that it is responsible for a majority of the relative wavelength selection in these two proteins (*17*). On the basis of the spectra shown in Figure 3 of ref *17*, the following long-wavelength absorption maxima at pH 9 are observed: BPR (486 nm), BPR-Q106L (510 nm), GPR (520 nm), and GPR-L105Q (497 nm). Thus, Gln-106 generates a blue shift of ~0.12 eV (11 kJ/mol) with a surprising consistency (±0.1 eV) with respect to the system. We explore the electrostatic and bonding nature of this blue shift and the structural relevance of this consistency in this section.

In all of the homology models that were generated, regardless of parent, minimization or dynamics generated structures in which Gln-106 was located above the chromophore in close proximity to the proton on C_{15}. In a majority of cases and with consistency for the SRII-based models, the carbonyl group of Gln-106 formed a hydrogen-bonding interaction with the proton on C_{15} as shown in Figure 10. This provides a significant stabilization to the ground state, but this observation does not provide an explanation for the blue shift in the absorption spectrum. The strength of this hydrogen bond is nearly identical in both the ground and excited singlet states. The origin of the blue shift is due to the large shift of electron density toward the imine linkage upon excitation into the low-lying, strongly allowed $^1B_u{}^{*+}$-like S_1 state. Because of the close proximity of the carbonyl oxygen of Gln-106 to this region, charge–charge interactions are less favorable in the S_1 excited state ($E_{stabilization} = -16.4$ kJ/mol) than in the ground state ($E_{stabilization} = -26.3$ kJ/mol). The calculated difference of 9.9 kJ/mol is very close to the observed blue shift of 11 kJ/mol and suggests that the primary source of the Q106 blue shift is due to electrostatic interactions between the chromophore and Q106. This observation suggests that as long as Gln-106 is oriented with the carbonyl oxygen atom directed toward the imine linkage it will induce a blue shift, and thus, the existence of a strong hydrogen bond between Gln-106 and the C15 hydrogen is not a critical component to this electrostatic effect. The hydrogen bond does, however, enhance the blue shift by holding Gln-106 in an optimal orientation to enhance the electrostatic effect.

Mechanism of the pH-Induced Spectral Shift. As shown in Figure 1, the absorption spectrum of BPR displays a marked pH dependence with a long-wavelength absorption maximum at ~540 nm at neutral to acidic pH and a maximum at ~493 nm in basic (pH > 10) solution. Although baseline problems because of protein–protein association at low pH make it difficult to observe a stable isosbestic point, SVD analysis of the spectra suggests that all of the spectra can be generated as a linear combination of two and only two species with maxima at ~493 and ~540 nm (see the Results). However, the aromatic region near 280 nm is more complicated, and SVD suggests that three aromatic residues may be influenced by changes in pH. In this section, we propose a tentative mechanism for the pH-induced spectra shift.
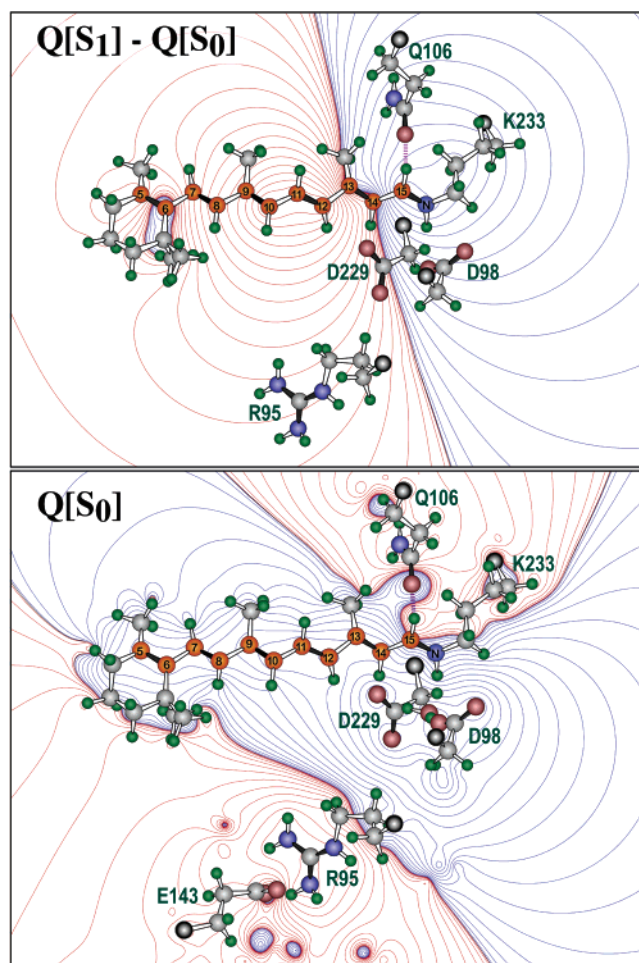

FIGURE 9: MNDO-PSDCI electrostatic contour maps in the plane of the polyene portion of the chromophore in the ground state (bottom) and associated with excitation into the lowest lying strongly allowed excited singlet state (top). Only selected residues are shown. The red lines show fields associated with a positive charge, and blue lines show fields associated with a negative charge. $Q[S_0]$ contours are drawn at ±26 200, ±22 400, ±19 100, ±16 100, ±13 400, ±11 000, ±8970, ±7180, ±5650, ±4350, ±3270, ±2380, ±1670, ±1120, ±706, ±409, ±209, ±88, ±26, ±3, and 0 J/mol, and $Q[S_1] - Q[S_0]$ contours are drawn at ±10 700, ±9150, ±7780, ±6550, ±5460, ±4500, ±3660, ±2930, ±2300, ±1780, ±1330, ±972, ±683, ±457, ±288, ±167, ±85, ±36, ±11, ±1, and 0 J/mol.

A glutamic acid at position 143 lies relatively close to the extracellular surface, and the protonation state of this residue will be sensitive to the pH of the aqueous medium. This residue lies closer to the β-ionylidene ring than to the imine nitrogen of the chromophore. (Our SRII-based model of BPR predicts that the Arg-95 residue forms a salt bridge with Glu-143 (−) in the resting state of the protein and that Glu-143 is therefore negatively charged under most conditions.) If all other structural details are kept constant, a negatively charged Glu-143 residue will generate a red shift because it provides preferential stabilization of the excited singlet state. This follows from the fact that Glu-143 resides within the positive region associated with the electrostatic potential induced via electronic excitation into the strongly allowed $^1B_u{}^{*+}$-like S_1 state (Figure 9). Thus, as the negative charge shifts toward the imine nitrogen upon excitation, the more positive β-ionylidene ring will experience enhanced stabilization from Glu-143 (−) and the energy of the excited state will be reduced (hence, a red shift). In practice, however,
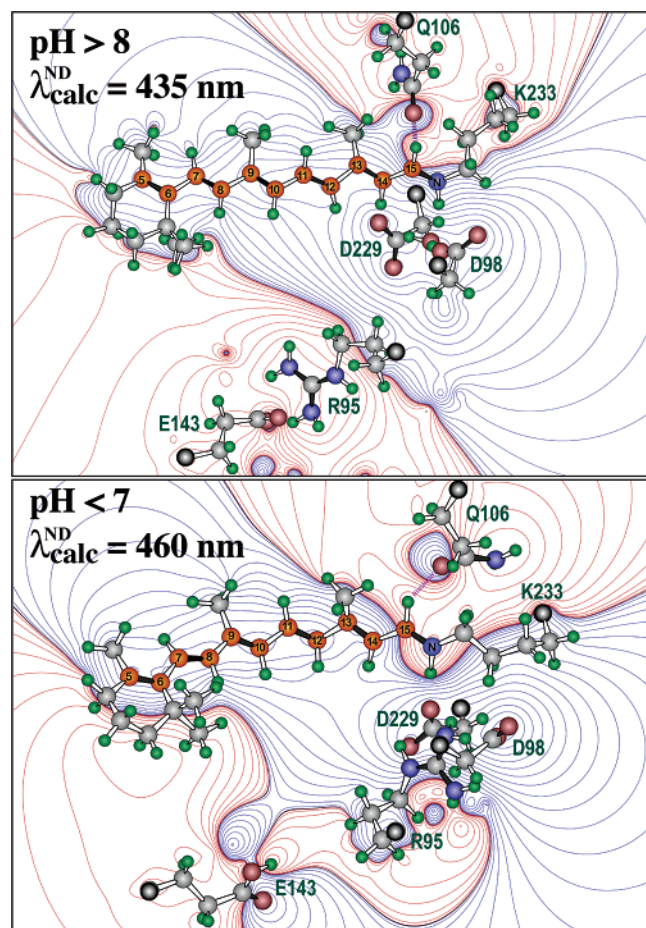
FIGURE 10: One possible model for the effect of pH on the absorption maximum of BPR. At high pH (top), Arg-95 (R95) and Glu-143 (E143) form a salt bridge. At low pH (bottom), E143 is protonated, thereby releasing R95 to seek electrostatic stabilization by forming a quadrapole with D98, D229, and K233 as shown in the lower figure. The MNDO-PSDCI calculations predict that this will lead to a red shift (see the text). The red lines show fields associated with a positive charge, and blue lines show fields associated with a negative charge. Contours are drawn at ±26 200, ±22 400, ±19 100, ±16 100, ±13 400, ±11 000, ±8970, ±7180, ±5650, ±4350, ±3270, ±2380, ±1670, ±1120, ±706, ±409, ±209, ±88, ±26, ±3, and 0 J/mol.

this residue is too distant from the chromophore to induce a significant spectral shift, and MNDO-PSDCI calculations indicate that the net red shift because of Glu-143 (−) is only −0.01 eV (red shift of ∼2 nm). However, if Glu-143 is protonated at neutral or acidic pH, the Arg-95 residue becomes destabilized and our dynamics calculations predict that it will move upward into the binding site near Asp-98 and Asp-229, both of which are negatively charged (see Figure 10).

The translocation of Arg-95 up into the binding site induces a red shift of 0.16 eV based on MNDO-PSDCI calculations (see Figure 10). This red shift is comparable to the observed red shift of 0.22 eV (493−540 nm, Figure 1); as such, the concerted coupling of the protonation of Glu-143 with the upward motion of Arg-95 into the binding site may be the key molecular event responsible for the pH-induced spectral shifts illustrated in Figure 1. The fact that the pH effect on the 280 nm band is complex and the SVD analysis indicates at least three separate components is consistent with a rearrangement involving Arg-95. There are

a number of Trp and Tyr residues near Arg-95 that will experience a change in the electrostatic field when this residue shifts from a down to an up position. When this residue is down (top of Figure 10), Arg-95 is in close proximity to Trp-99 (2.9 Å), Tyr-96 (3.1 Å), and Tyr-225 (4.1 Å). These three residues experience a change in the electrostatic field when Arg-95 shifts up into the binding site, although Arg-95 remains relatively close to Trp-99 but shifts close to NE1. All three of these residues will have their absorption spectra subtly shifted by the motion of Arg-95 nearby, and thus, the complex SVD associated with decomposition of the 280 nm band is consistent with the model shown in Figure 10.

COMMENTS AND CONCLUSIONS

This investigation concludes that the structure and electronic properties of an SRII-based homology model of BPR are more realistic than those predicted on the basis of the more traditional BR-based structures (*17*). First, we note that the retinal-binding site of our BR-based homology model is not stable to long-term dynamics simulations because the binding site spontaneously collapses to generate a salt bridge between the chromophore and Asp-229. The calculated spectroscopic properties of this collapsed binding site yield an unrealistic excited-state level ordering and an absorption spectrum with a significant hypochromic shift of the strongly allowed λ_{max} band. The dynamics simulations performed on the SRII-based homology model yield a more stable counterion complex, with Asp-229 positioned more than 3.0 Å from the protonated Schiff-base linkage of the chromophore. The stability of the SRII-based binding pocket contributed to more realistic spectroscopic properties.

The observation that SRII provides a better homology parent than BR raises the question of whether BPR is a proton pump or a sensory pigment *in vivo*. The most important experimental evidence in support of the proton-pump assignment is the work of Wang et al., who demonstrated that BPR carries out light-driven proton transport in *E. coli* vesicles, albeit with a reduced rate of translocation (*27*). The inefficient rate of proton translocation may be attributed to the slow photokinetics of the BPR photocycle, relative to BR and GPR. Structural models of BPR also show the presence of a glutamic acid (109) at a position that is analogous to the primary proton-donor group in BR (Asp-96). The presence of Glu-109 on the cytoplasmic side of BPR, in conjunction with Glu-143 on the extracellular side, further supports the idea that BPR is pumping protons via a channel of ionic residues. All of these observations support the proton-pump assignment.

However, we note some issues that must be resolved prior to concluding that BPR is not a sensory pigment. First, the observation that BPR pumps protons is not unto itself meaningful. In the absence of its transducer protein, HtrII, SRII has also been shown to display an apparent proton-pumping activity and a photochemical reaction cycle that mimics BPR in efficiency (*23*). However, SRII does not actually translocate protons but circulates them on the extracellular side of the membrane (*23*). The circulation of protons by SRII may be attributed to the lack of a proton channel, common to both BR and halorhodopsin (HR).

We conclude that BPR is most likely a proton pump, but this assignment cannot be made with certainty. If a transducer

protein (analogous to HtrII) for BPR was discovered, it would obviously alter this view. However, the majority of the available evidence supports the concept that BPR is serving an energy-harvesting function via proton translocation.

We conclude by asking the following question: if BPR is a proton pump, then why is SRII a better homology model than BR for BPR? We believe there are two likely answers. First, SRII and BPR have λ_{max} absorption bands that are relatively similar, and while the mechanisms are not identical, the SRII-based structure may be a better model for a blue-shifted chromophore. Second, BPR and SRII share an important characteristic in the extracellular region. Both BPR and SRII have only a single glutamic acid residue in the central extracellular region, and in terms of location, Glu-143 in BPR appears to be better described in terms of properties and interactions by the single Asp-193 residue in SRII than the Glu-194 and Glu-204 pair in BR. We suggest that SRII may provide a better structural template for all blue-shifted retinal proteins, rather than BPR in particular.

REFERENCES

1. Allinger, N. L. (1977) Conformational analysis. 130. MM2. A hydrocarbon force field utilizing V1 and V2 torsional terms, *J. Am. Chem. Soc. 99*, 8127−8134.
2. Allinger, N. L., and Burkert, U. (1982) *Molecular Mechanics*, American Chemical Society, Washington, DC.
3. Allinger, N. L., Kuang, J., and Thomas, H. D. (1990) Molecular mechanics (MM2 and MM3) calculations on aliphatic and aromatic nitro compounds, *Theochem. 68*, 125−148.
4. Allinger, N. L., Yuh, Y. H., and Lii, J. H. (1989) Molecular mechanics. The MM3 force field for hydrocarbons, *J. Am. Chem. Soc. 111*, 8551−8566.
5. Béjà, O., Aravind, L., Koonin, E., Suzuki, M., Hadd, A., Nguyen, L., Joanovich, S., Gates, C., Feldman, R., Spudich, J., Spudich, E., and DeLong, E. (2000) Bacterial rhodopsin: Evidence for a new type of phototrophy in the sea, *Science 289*, 1902−1906.
6. Béjà, O., Spudich, E., Spudich, J., Leclerc, M., and DeLong, E. (2001) Proteorhodopsin phototrophy in the ocean, *Nature 411*, 786−789.
7. Bergo, V., Amsden, J. J., Spudich, E. N., Spudich, J. L., and Rothschild, K. J. (2004) Structural changes in the photoactive site of proteorhodopsin during the primary photoreaction, *Biochemistry 43*, 9075−9083.
8. Brooks, B., Bruccoleri, R. E., Olafson, B. D., States, D. J., Swaminathan, S., and Karplus, M. (1983) CHARMM: A program for macromolecular energy, minimization, and dynamics calculations, *J. Comput. Chem. 4*, 187−217.
9. Dioumaev, A., Brown, L., Shih, J., Spudich, E., Spudich, J., and Lanyi, J. (2002) Proton transfers in the photochemical reaction cycle of proteorhodopsin, *Biochemistry 41*, 5348−5358.
10. Henikoff, S., and Henikoff, J. G. (1992) Amino acid substitution matrices from protein blocks, *Proc. Natl. Acad. Sci. U.S.A. 89*, 10915−10919.
11. Henikoff, S., Henikoff, J. G., and Pietrokovski, S. (1999) Blocks+: A non-redundant database of protein alignment blocks derived from multiple compilations, *Bioinformatics 15*, 471−479.
12. Hermone, A., and Kuczera, K. (1998) Free-energy simulations of the retinal cis−trans isomerization in bacteriorhodopsin, *Biochemistry 37*, 2843−2853.
13. Kelemen, B. R., Du, M., and Jensen, R. B. (2003) Proteorhodopsin in living color: Diversity of spectral properties within living bacterial cells, *Biochim. Biophys. Acta 1618*, 25−32.
14. Kusnetzow, A. K., Dukkipati, A., Babu, K. R., Ramos, L., Knox, B. E., and Birge, R. R. (2004) Vertebrate ultraviolet visual pigments: Protonation of the retinylidene Schiff base and a counterion switch during photoactivation, *Proc. Natl. Acad. Sci. U.S.A. 101*, 941−946.
15. Lakatos, M., and Varo, G. (2004) The influence of water on the photochemical reaction cycle of proteorhodopsin at low and high pH, *J. Photochem. Photobiol., B 73*, 177−182.
16. Luecke, H., Schobert, B., Richter, H. T., Cartailler, J. P., and Lanyi, J. K. (1999) Structure of bacteriorhodopsin at 1.55 Å resolution, *J. Mol. Biol. 291*, 899−911.
17. Man, D., Wang, W., Sabehi, G., Aravind, L., Post, A. F., Massana, R., Spudich, E. N., Spudich, J. L., and Beja, O. (2003) Diversification and spectral tuning in marine proteorhodopsins, *EMBO J. 22*, 1725−1731.
18. Martin, C. H., and Birge, R. R. (1998) Reparameterizing MNDO for excited-state calculations using *ab initio* effective Hamiltonian theory: Application to the 2,4-pentadien-1-iminium cation, *J. Phys. Chem. A 102*, 852−860.
19. Ren, L., Martin, C. H., Wise, K. J., Gillespie, N. B., Luecke, H., Lanyi, J. K., Spudich, J. L., and Birge, R. R. (2001) Molecular mechanism of spectral tuning in sensory rhodopsin II, *Biochemistry 40*, 13906−13914.
20. Royant, A., Nollert, P., Edman, K., Neutze, R., Landau, E. M., Pebay-Peyroula, E., and Navarro, J. (2001) X-ray structure of sensory rhodopsin II at 2.1 Å resolution, *Proc. Natl. Acad. Sci. U.S.A. 98*, 10131−10136.
21. Sabehi, G., Beja, O., Suzuki, M. T., Preston, C. M., and DeLong, E. F. (2004) Different SAR86 subgroups harbour divergent proteorhodopsins, *Environ. Microbiol. 6*, 903−910.
22. Sabehi, G., Massana, R., Bielawski, J. P., Rosenberg, M., DeLong, E., and Beja, O. (2003) Novel proteorhodopsin variants from the mediterranean and red seas, *Environ. Microbiol. 5*, 842−849.
23. Sasaki, J., and Spudich, J. L. (2000) Proton transport by sensory rhodopsins and its modulation by transducer-binding, *Biochim. Biophys. Acta 1460*, 230−239.
24. Shima, S., Ilagan, R. P., Gillespie, N., Sommer, B. J., Hiller, R. G., Sharples, F. P., Frank, H. A., and Birge, R. R. (2003) Two-photon and fluorescence spectroscopy and the effect of environment on the photochemical properties of peridinin in solution and in the peridinin-chlorophyll-protein from *Amphidinium carterae*, *J. Phys. Chem. A 107*, 8052−8066.
25. Spudich, J., and Luecke, H. (2002) Sensory rhodopsin II: Functional insights from structure, *Curr. Opin. Struct. Biol. 12*, 540−546.
26. Teodorescu, O., Galor, T., Pillardy, J., and Elber, R. (2004) Enriching the sequence substitution matrix by structural information, *Proteins: Struct., Funct., Bioinf. 54*, 41−48.
27. Wang, W. W., Sineshchekov, A., Spudich, E., and Spudich, J. (2003) Spectroscopic and photochemical characterizatin of a deep ocean proteorhodopsin, *J. Biol. Chem. 278*, 33985−33991.